Journal of Infrared, Millimeter, and Terahertz Waves (2022) 43:709–727
https://doi.org/10.1007/s10762-022-00882-2

INVITED REVIEW ARTICLE

Progress in performance development of room temperature direct terahertz detectors

A. Rogalski[1]

Received: 26 October 2021 / Accepted: 5 October 2022 / Published online: 4 November 2022

Abstract
In this paper issues, associated with the development of THz direct detectors and focal plane arrays in the last decade are discussed. After short description of general classification of THz detectors, more details concern Schottky barrier diodes, CMOS-based detectors, microbolometers, and field-effect transistor detectors, where links between THz devices and modern technologies such as micromachining are underlined. Special attention has been paid to the development of detectors made of two-dimensional materials. Their performance is comparable to that presented for classical terahertz detectors. It is shown that applications of nanoscale materials and devices, in particular, made of two-dimensional materials, open the door for further performance improvement of THz detectors operated at room temperature.

Keywords Thermal detectors · Photon detectors · 2D material photo detectors · Uncooled focal plane arrays

1 Introduction

The development of THz technology started in the 1980s mainly for laboratory applications (see Fig. 1). It was an expensive scientific device that could only be used by highly trained personnel. However, over the last two decades, efforts have been made to implement easy-to-use and cost-effective systems by developing more compact and reliable components. Now, THz techniques are entering the commercial market, and the first products for applications such as industrial process monitoring on the production line have already been sold.

The total size of the THz market appears to be difficult to determine. The market reports differ in their estimates for 2020 by more than a factor of 4 (Fig. 2). According to a French research firm, Tematys, the total market is about 100 USD million [2,

✉ A. Rogalski
antoni.rogalski@wat.edu.pl

[1] Institute of Applied Physics, Military University of Technology, 2 Kaliskiego St, 00-908 Warsaw, Poland

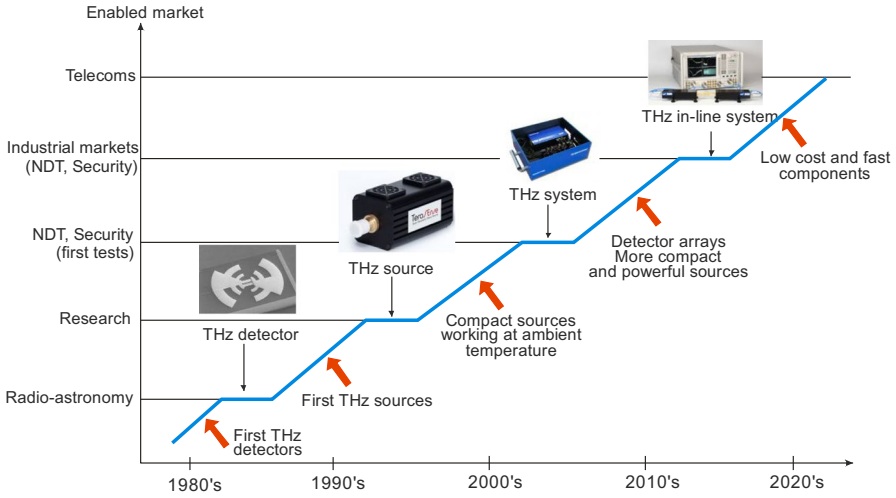

Fig. 1 Development of THz technologies (reprinted with permission from Tematys [1])

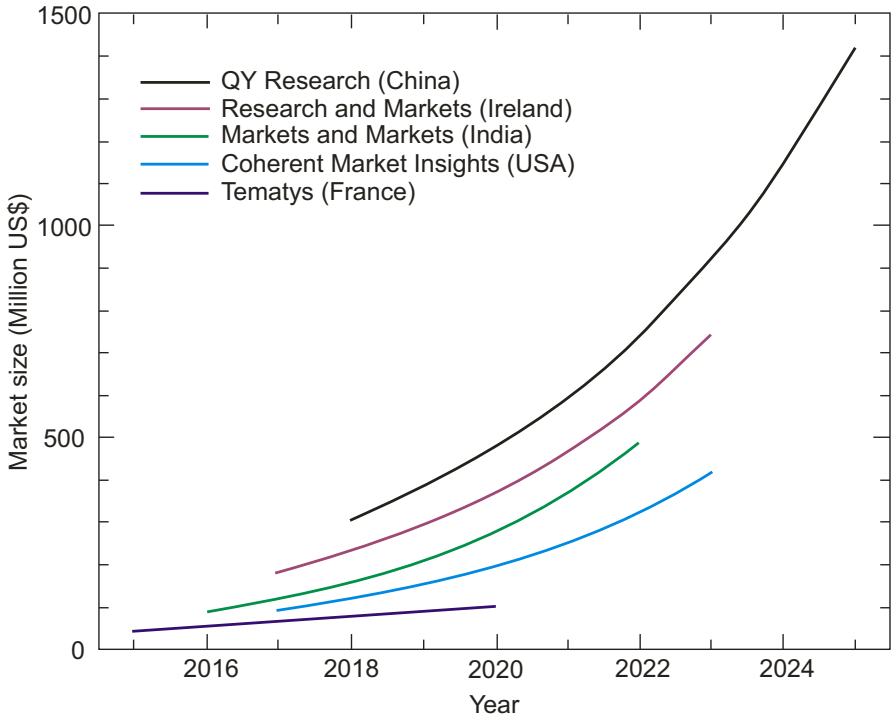

Fig. 2 Global terahertz market according to five different analyst firms (reproduced from Naftaly et al. [2])

3]. At the other end of the spectrum is Beijing-based QY Research, which believes that the current market size is $385 million [4]. Similarly, forecasts for the annual growth rate (CAGR) vary by a factor of two, with values ranging from 16 (Tematys) to nearly 32% (QY Research). From Fig. 2 results that a simple arithmetic average from the global market five reports, is approximately 230 million US$ in 2020. All reports agree that the THz technology market will continue to grow, and even the most pessimistic forecast CAGR of 16% still indicates significant growth.

2 General Classification of Terahertz Detectors

The terahertz (THz) detectors are generally classified in two broad categories: thermal detectors and photon detectors. Their operation principled is briefly described in Table 1.

THz detector should be characterized by high sensitivity, short response time, low-power consumption, and compatibility with the electronic input circuit, as well as operational reliability, high quantum efficiency, good thermal properties, low dark current, low noise, long lifetime, small size, and low manufacturing costs. In the following, we will define some important parameters that characterize terahertz detectors and their detector arrays.

Table 1 Operation principles of THz detectors

Mode of operation	Schematic of detector	Operation and properties
	Thermal detectors	
Thermopile	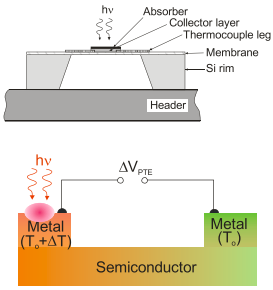	The thermocouple is usually a thin, blackened flake connected thermally to the junction of two dissimilar metals or semiconductors. Heat absorbed by the flake causes a temperature rise of the junction, and hence a thermoelectric electromotive (the Seebeck effect) force is developed which can be measured. Although thermopiles are not as sensitive as bolometers and pyroelectric detectors, they will replace these in many applications due to their reliable characteristics and good cost/performance ratio. A derivative of this effect is the photo-thermoelectric (PTE) effect. This effect is based on the thermoelectric effect caused by non-uniform light illumination. It can be also created by strong difference in the absorption in distinct parts of the device under global illumination. The adjacent figure illustrates the light induced heating effect in semiconductor channel (e.g. in a field-effect transistor), which leads to a temperature gradient.
Bolometer	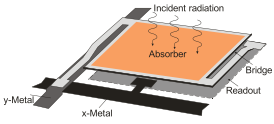	The bolometer is a resistive element constructed from a material with a very small thermal capacity and large temperature coefficient so that the absorbed radiation produces a large change in resistance. The change in resistance is like the photoconductor; however, the basic detection mechanisms are different. In the case of a bolometer, radiant power produces heat within the material, which in turn produces the resistance change. There is no direct photon-electron interaction. At present microbolometers are fabricated in large format arrays for imaging applications.
Pyroelectric detector	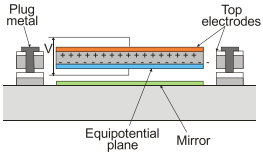	The pyroelectric detector can be considered as a small capacitor with two conducting electrodes mounted perpendicularly to the direction of spontaneous polarization. During incident of radiation, the change in polarization appears as a charge on the capacitor and a current is generated, the magnitude of which depends on the temperature rise and the pyroelectrical coefficient of the material. The signal, however, must be chopped or modulated. The detector sensitivity is limited either by amplifier noise or by loss-tangent noise. Response speed can be engineered making pyroelectric detectors useful for fast laser pulse detection, however with proportional decrease in sensitivity.

Table 1 (continued)

Golay cell	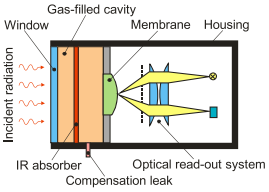	The Golay cell consists of a hermetically sealed container filled with gas (usually xenon for its low thermal conductivity) and arranged so that expansion of the gas under heating by a photon signal distorts a flexible membrane. The deflection of the membrane can be read by an optical system, a capacitive detector, or a tunneling displacement transducer. To enhance the infrared absorption in the gas, the cavity is equipped with an additional absorber. Another way to enhance absorption is to use reflective walls of the cavity. The temperature changes of the gas caused by the absorbed IR radiation are in the range of mK. The performance of the Golay cell is only limited by the temperature noise associated with the thermal exchange between the absorbing film and the detector gas; consequently, the detector can be extremely sensitive with $D^* \approx 3\times10^9$ cmHz$^{1/2}$W^{-1}, and responsivities of 10^5 to 10^6 V/W. The response time is quite long in msec range.
Photon detectors		
Photoconductor	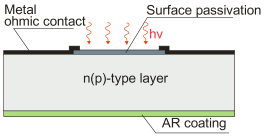	It is substantially photoresistor sensitive to optical radiation; the incident radiation creates electrons or holes in a uniform bulk semiconductor material. An intrinsic photoconductor utilizes the absorption of a photon with sufficient energy as to create an electron-hole pairs directly across the bandgap of the semiconductor. The spectral response in this case is determined primarily by the bandgap. An extrinsic photoconductor depends upon the ionization of impurities in the semiconductor and in this case only one carrier type, either electrons or holes, is active. The extrinsic spectral response is determined by the ionization energy of impurities.
Hybrid photoconductor	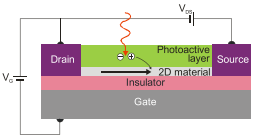	The hybrid phototransistor is very popular in a design of 2D material photodetectors with the fast transfer channel for charge carriers. Since, e.g. graphene or other 2D material in these devices is not responsible for light absorption but only for charge sensing, the absorber choice determines the spectral response. The 2D material large ambipolar mobility acts as a built-in photogain (i.e., amplifier) mechanism enhancing the detector response. 2D materials with thickness down to atomic layer are more susceptible to local electric fields than conventional bulk materials and the photogating effect can strongly modulate the channel conductivity by the external gate voltage, V_G. In this way, ultra-high gain up to 10^8 electrons per photon and exceptional responsivities for short wavelength infrared photodetectors have been demonstrated.
p-n junction	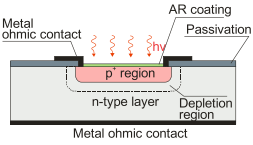	Normally a p-on-n configuration consists of a shallow diffused p-region to the n-type active layer, although n-on-p design is also available. Photons with energy greater than the energy gap of semiconductor create electron-hole pairs on both sides of the junction. By diffusion, carriers generated within a diffusion length from the junction reach the space-charge region where they are separated by the electric field (minority carriers become majority carriers on the other side). This way a photocurrent is generated causing a change in voltage across the open-circuit cell or a current to flow in the short-circuited case.
Schottky barrier photodiode	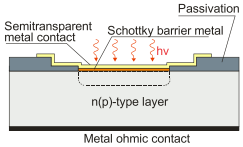	This photovoltaic detector is a majority carrier device formed at a metal-semiconductor junction. Like p-n junction, metal-semiconductor interface provides a potential barrier which separates photoexcited electron-hole pairs. Photoexcitation can occur within the semiconductor or at the metal-semiconductor interface. Schottky barrier photodiode reveal some advantages over p-n junction photodiode: fabrication simplicity (deposition of metal barrier on n(p)-semiconductor), absence of high-temperature diffusion processes, and high speed of response.
FET detector	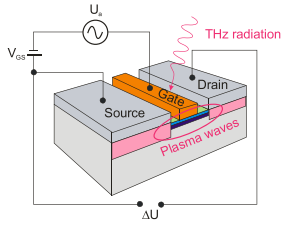	The detection by FETs is due to nonlinear properties of the transistor leading to the rectification of the AC current induced by the radiation where photoresponse appears in the form of a DC voltage between source and drain and is proportional to the radiation intensity (PV effect). In the resonant regime, the plasma waves are dimly damped (when a plasma wave launched at the source can reach the drain in a time shorter than the momentum relaxation time) and the detection mechanism exploits interference of the plasma waves in the cavity, resulting in a resonantly enhanced response. An improvement in sensitivity can be reached by adding a proper antenna or a cavity coupling. Broadband detection occurs when plasma waves are overdamped (meaning when plasma waves launched at the source decay before reaching the drain).

Responsivity is defined as the output signal (typically voltage or current) of the detector produced in response to a given incident radiant power falling on the detector.

Noise equivalent power (*NEP*) is the incident power on the detector that produces a signal-to-noise ratio of unity at the output of a given optical detector at a given data-signaling rate or modulation frequency, operating wavelength, and effective noise bandwidth. Some manufacturers and authors define *NEP* as the minimum detectable power per square root bandwidth [W/Hz$^{1/2}$].

In terms of responsivity, it can be written:

$$NEP = \frac{V_n}{R_v} = \frac{I_n}{R_i}. \tag{1}$$

where V_n and I_n are voltage and current noises and R_v and R_i are voltage and current responsivities. The unit of *NEP* is the watt.

The *NEP* is also quoted for a fixed reference bandwidth which is often assumed to be 1 Hz. This "*NEP* per unit bandwidth" has a unit of watts per square root Hertz (W/Hz$^{1/2}$). The *NEP* depends on the optical wavelength, as well, since the detector responsivity is wavelength dependent.

The normalized detectivity D^* (or *D*-star) is related to the unit detector area and the unit bandwidth. This means that both *NEP* and detectivity are functions of the electrical bandwidth, Δf, and detector area, A_d:

$$D^* = D\left(A_d \Delta f\right)^{1/2} = \frac{\left(A_d \Delta f\right)^{1/2}}{NEP} \tag{2}$$

It is the most important detector parameter which allows the comparison of the same type detectors but having different areas. D^* is expressed in the unit of cmHz$^{1/2}$/W which is more commonly called "Jones."

Noise equivalent difference temperature (*NEDT*) is a fundamental figure of merit for focal plane arrays (FPAs) and characterizes the thermal sensitivity of a system. It can be defined as the amount of temperature difference required to produce a unity signal-to-noise (S/N) ratio. *NETD* is defined as:

$$NETD = \frac{V_n}{\Delta V / \Delta T}, \tag{3}$$

where V_n is the noise and ΔV represents the signal measured for the temperature difference ΔT. *NETD* characterizes the detection system sensitivity for low spatial frequencies. A smaller *NEDT* value indicates a better thermal sensitivity.

Table 2 compares the general performance of the state-of-the-art THz detectors in terms of their operating frequency, speed, responsivity, and noise equivalent power.

3 Uncooled Direct THz Detectors

The performance of different types of THz detectors operating at room temperature is summarised in Table 3 [5]. As we see, the spread in detector parameters is large. The sensitivity parameter only partially characterizes the detector. *NEP* is much

Table 2 Uncooled THz detectors performance comparison

THz detector	Response speed	Frequency [THz]	Responsivity [kV/W]	*NEP* [pW/Hz$^{1/2}$]
Golay cell	Slow (50 ms)	0.04–30	10–100	140
Pyroelectric detector	Slow (100 ms)	0.2–30	20–400	1000
Bolometer	Moderate (1 ms)	0.1–30	100–1000	0.1
SBDs	Fast (20 ps)	0.1–10	1	1–50
FET	Fast	0.1–8	0.1–0.4	10–100
Graphene FET	Fast	0.1–3	0.05–0.1	500–900

more important from the detector system point of view—there is a lot of experimental data on *NEP* for rectifier detectors. In the last decade CMOS detectors, microbolometers and plasma detectors have been growing rapidly, indicating that these technologies are widely available. The data for pyroelectric detectors and Golay cells are the most sparse of all.

The performance results to date for different detector type are compared in the bar chart of Fig. 3. We chose the frequency range close to 650 GHz since it is the center frequency located in a well-known window useful for terrestrial sensing (at higher frequency the atmosphere is prohibitively lossy). As is shown, the Si-CMOS and SiGe-based devices are characterized by *NEP* values around 50 pW/Hz$^{1/2}$. For pyroelectric detectors and Golay cells, the *NEP* values lie above 100 pW/Hz$^{1/2}$ and close to 1 nW/Hz$^{1/2}$. Schottky-barrier detectors (SBDs) respond to the THz electric field and usually generate an output current or voltage through a quadratic term in their current–voltage characteristics. In general, the *NEP* of SBD and FET detectors is better than that of Golay cells and pyroelectric detectors around 650 GHz. Both the pyroelectric and the bolometer FPAs with detector response times in the millisecond range are not suitable for heterodyne operation. FET detectors are clearly capable of heterodyne detection with improved sensitivity. 2D materials like graphene and black phosphorus (bP) (FET and PTE detectors) are promising materials for the development of room temperature detectors operating across the FIR in spectral range above 100 μm (at frequency below 3 THz).

4 2D Materials in THz Detector Family

Since the discovery of graphene, intensive research has begun on 2D materials for their potential applications as photodetectors over a wide range of the electromagnetic spectrum. Most of the research has been devoted to photon detectors in the visible and NIR range. However, a more interesting range of potential applications for these materials is the terahertz range.

It is well-known that the performance of photodetectors mainly depends on the properties of the photodetector active regions, such as absorption coefficient, e–h pair lifetime, and charge mobility [6]. The high dark current of conventional

Table 3 Parameter of some uncooled THz detectors

Device type	Electrical responsivity (V/W)	Conditions	*NEP* (W/Hz$^{1/2}$)
Schottky diodes			
ErAs/InGaAlAs spiral planar antenna	-	Zero bias, 639 GHz	4.0×10^{-12} *NEDT* = 120 mK
InGaAs log-spiral antenna	~200 for system estimate 10^3 intrinsic for the diode	0.8 THz	5.0×10^{-12}
VDI Model: WR2.8 ZBD	1500	260–400 GHz	2.7×10^{-12}
VDI Model:WR1.5ZBD	750	500–750 GHz	5.1×10^{-12}
VDI Model: WR1.0 ZBD	200	750–1100 GHz	20×10^{-12}
VDI Model:WR0.65 ZBD	100	1100–1700	40×10^{-12}
Bolometers			
$Hg_{0.8}Cd_{0.2}Te$ HEB	0.30 at 17 mV bias, 36 GHz 96 for 0.89 THz, 13 mV bias	Room temperature	2.2×10^{-9} for 17 mV bias, 35 GHz 7.4×10^{-9} for 0.89 THz, 12 mV bias
Si_xGe_y:H	170	0.934 THz, uncooled	0.2×10^{-9}
Vanadium oxide	-	Uncooled	320×10^{-12} at 4.3 THz, 9×10^{-13} @ 7.5–14 μm
Niobium film	21	3.6 mA bias, 1 kHz mod, 300 K	1.10×10^{-10}
Ti, antenna-coupled microbolometer	-	10 kHz chop, 1.04 mA bias, 300 K	1.5×10^{-11}
Nb_5N_6	400	0.4 mA bias, > 10 kHz	9.8×10^{-12}
Vanadium oxide array	1.5×10^4	1 V bias, 130 μm, uncooled	2.00×10^{-10}
Nb, polymide, antenna coupled	450	< 1 THz	1.5×10^{-11}
Al/Nb; antenna coupled	85	1 kHz mod, 1.6 mA bias	2.5×10^{-11}
Fee-standing Nb bridge antenna coupled	210 (average over 10 devices)	650 GHz	12.5×10^{-12}
Pyroelectrics			
Philips P5219 deuterated L-alanine TGS	321	10 Hz mod; amplifier with gain of 4.8, 91 GHz	3.1×10^{-8}
QMC instr	18, 300 1200	10 Hz mod; 1.89 THz, < 20 Hz mod	4.4×10^{-10}

Table 3 (continued)

Device type	Electrical responsivity (V/W)	Conditions	*NEP* (W/Hz$^{1/2}$)
$LiTaO_3$	-	530 GHz, Melectron Model SPH-45	2.0×10^{-9}
Golay cells			
Tydex Golay cell GC-1X	100, 000	21 Hz chopper	1.4×10^{-10}
Microtech instruments	10, 000	12.5 Hz chopper	10×10^{-8}
Micro-array, layer by layer, polymer membranes over Si	-	30 Hz mod 105 GHz	300×10^{-9}
Tydex Golay cell, 6-mm-diameter diamond window		10 Hz mod	7.0×10^{-10}
CMOS-based and plasma detectors			
BiCMOS SiGe, 0.25 µm HBT	Current R_i 1 A/W at 0.7 THz	3×5 array, chopper 125 kHz	50×10^{-12} at 0.7 THz
BiCMOS SiGe, 0.25 µm NMOS	Voltage R_v 80 kV/W at 0.6 THz	3×5 array, chopper 16 kHz	300×10^{-12} at 0.6 THz
CMOS SiGe, 65 nm NMOS	Voltage R_v 140 kV/W at 0.87 THz	32×32 array, chopper 5 kHz	100×10^{-12} at 0.87 THz
CMOS SiGe, 65 nm NMOS	Voltage R_v 0.8 kV/W at 1 THz	3×5 array, chopper 1 kHz	66×10^{-12} at 1 THz
CMOS-SBD, 130 nm	Voltage R_v 0.323 kV/W at 0.28 THz	4×4 array, chopper 1 kHz	29×10^{-12} at 0.28 THz
CMOS-SBD, 65 nm	-	1 element; 1 MHz mod	42×10^{-12} at 0.86 THz
CMOS, 150 nm, NMOS	Voltage R_v at 4.1 THz	1 element	133×10^{-12} at 4.1 THz
InGaAs HEMT	Voltage R_v 23 kV/W at 200 GHz	1 element	0.5×10^{-12} at 200 GHz
Asymmetric dual-grating gate InGaAs HEMT	Voltage R_v 6.4 kV/W at 1.5 THz	1 element	50×10^{-12} at 1.5 THz

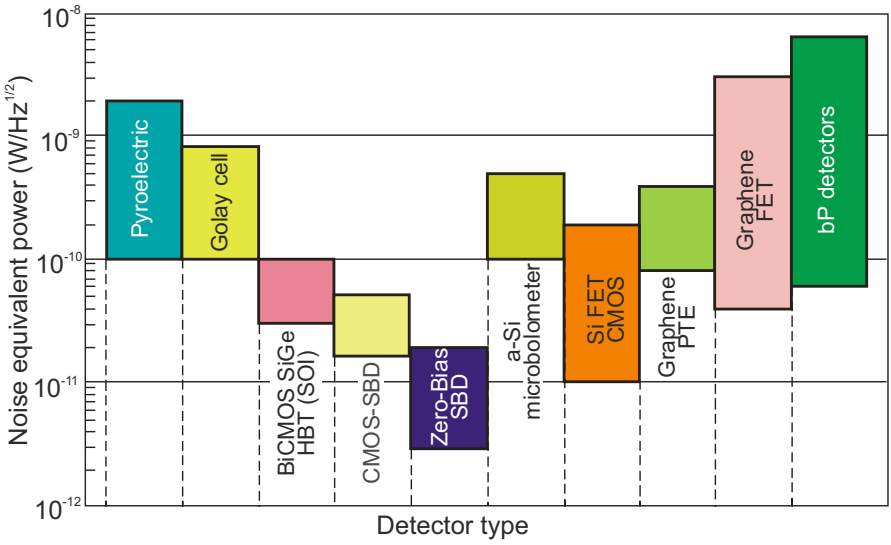

Fig. 3 Comparison of room-temperature direct detectors operating > 300 GHz. SOI, silicon on insulator; FET, filed effect transistor

graphene material, resulting from its gapless nature, significantly reduces the sensitivity of the photodetector and limits the further development of graphene-based photodetectors. From these reasons, the alternative 2D-based materials, like black phosphorus (bP), are considered.

Various sensing mechanisms are involved in 2D terahertz material detectors; the most important are bolometric effect, photothermoelectric effect (PTE), and plasma wave rectification in FET. Table 4 summarizes the performance of representative detectors [7].

Figure 4 compares *NEP* values of graphene-based and bP detectors with existing standard THz ones. Most of the experimental data collected in the literature are for single graphene detectors operating above 100 µm wavelength (frequency range below 3 THz). In general, the performance of graphene FET detectors is lower compared to CMOS and plasmonic detectors made of III-V Schottky-barrier and silicon-based materials, SiGe and InGaAs. However, compared to VO_x and amorphous silicon microbolometers, the performance of graphene detectors is close to the trend line estimated for microbolometers in the THz spectral region (see Fig. 5). The best quality VO_x bolometer arrays are characterized by lower *NEP* value of about 1 pW/Hz$^{1/2}$ in the LWIR range (≈ 10 µm). However, it should be noted here that the microbolometer data are for above megapixels monolithic arrays, what is big advantage of this monolithic infrared detector technology in comparison with THz range.

As Fig. 4 shows, black phosphor has emerged as candidate of 2D material for terahertz detection applications. However, surface instability due to chemical

Table 4 Terahertz detectors based on 2D materials

Mechanism	Material	Frequency	Responsivity	*NEP*	D^*	Response time	T	Ref
Bolometer	bP	~0.3 THz	7.8 V/W	4 nW/Hz$^{1/2}$	~1.2×10^7 Jones	< 1 ms	300 K	8
Bolometer	Graphene	0.3–1.6 THz	-	5.6 pW/Hz$^{1/2}$	~3.3×10^9 Jones	< 100 μs	3 K	9
Bolometer	Graphene	0.15 THz	5×10^{10} V/W	0.2 fW/Hz$^{1/2}$	~2.2×10^{12} Jones	< 2.5 ns	300 K	10
PTE	Graphene	2.52 THz	> 10 V/W	1.1 nW/Hz$^{1/2}$	~1.9×10^5 Jones	< 110 ps	300 K	11
PTE	Graphene	2 THz	> 4.9 V/W	1.7 nW/Hz$^{1/2}$	~2.2×10^6 Jones	< 50 ms	300 K	12
PTE	bP	~0.3 THz	> 0.15 V/W	40 nW/Hz$^{1/2}$	~1.2×10^6 Jones	< 2 ms	300 K	13
PTE	bP	~0.3 THz	> 1.1 V/W	45 nW/Hz$^{1/2}$	~1.0×10^6 Jones	< 2 ms	300 K	8
FET	Graphene	~0.3 THz	> 0.15 V/W	30 nW/Hz$^{1/2}$	~1.5×10^6 Jones	< 1 ms	300 K	14
FET	Graphene	~0.6 THz	> 14 V/W	515 pW/Hz$^{1/2}$	~4.9×10^7 Jones	< 30 μs	300 K	15
FET	Graphene	~0.3 THz	> 1.2 V/W	2 nW/Hz$^{1/2}$	~2.3×10^7 Jones	< 2.5 ms	300 K	16
FET	Graphene	~0.3 THz	> 30 V/W	163 pW/Hz$^{1/2}$	~3.0×10^8 Jones	< 5 μs	300 K	17
FET	bP	~0.3 THz	> 5 V/W	10 nW/Hz$^{1/2}$	~4.8×10^6 Jones	< 10 ms	300 K	8
FET	Graphene	230–375 GHz	> 0.25 V/W	10 nW/Hz$^{1/2}$	~5.8×10^5 Jones	< 1.2 ms	300 K	18
FET	Graphene	0.13 GHz	> 20 V/W	0.6 nW/Hz$^{1/2}$	~1.9×10^8 Jones	-	300 K	19
FET	bP	0.15 THz	> 300 V/W	1 nW/Hz$^{1/2}$	~1.7×10^6 Jones	< 4 μs	300 K	20
FET	Graphene	0.15 THz	> 400 V/W	0.5 nW/Hz$^{1/2}$	~3.5×10^8 Jones	< 20 μs	300 K	21

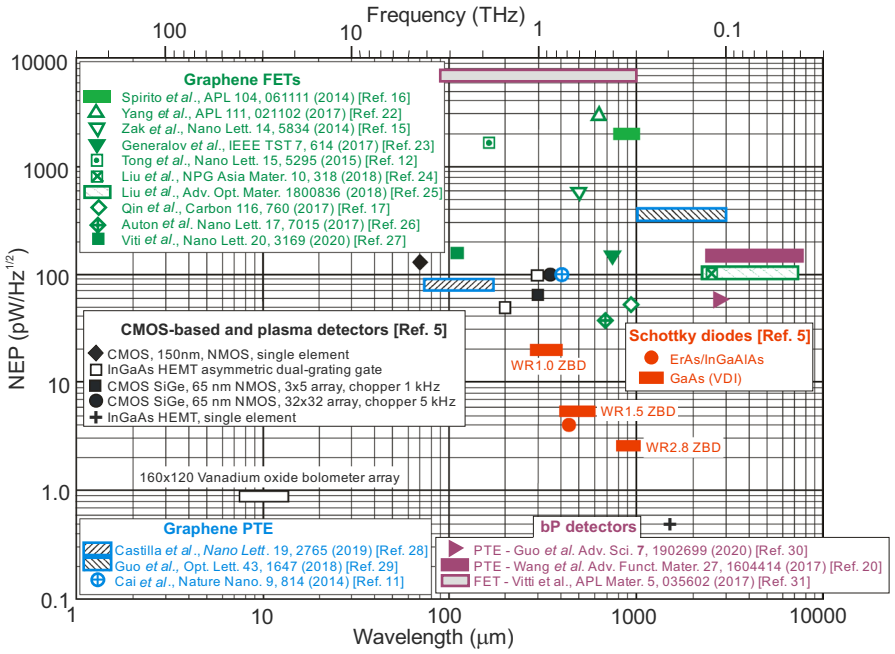

Fig. 4 NEP spectral dependence for graphene-based FET detectors and bP detectors with different standard photon THz ones (CMOS-based, Schottky diodes). The experimental data are taken from literature marked inside the figure

degradation under ambient conditions remains a major obstacle to it future applications [33, 34]

5 Uncooled THz Focal Plane Arrays in Active Imaging

There are two methods used in THz imaging: passive imaging and active imaging. The passive imaging uses the thermal radiation emitted by an object. Since the low-temperature objects emit very low power radiation, the THz detector sensitivity is required to be very high (*NEP* value on the order of several fW/$\sqrt{\text{Hz}}$), which can only be achieved using cryogenic or heterodyne detector systems. The manufacturing and operating costs as well as the size of these systems limit them to applications such as defense, space, and security. To omit these technological barriers, the uncooled THz active systems are manufactured with considerable lower costs. However, these systems require the use of external sources of illuminations.

The schematic arrangement of active THz imaging system is shown in Fig. 6. Most of the systems use monochromatic THz sources such as quantum cascade lasers (QCLs) or far infrared optically pumped lasers delivering mW-range powers. As is shown in Fig. 6, the reflected beam backlights an object with a maximum area, and the transmitted light is collected by a camera lens. The focal plane is positioned behind the camera lens, making the object plane in front of the lens. Also shown is

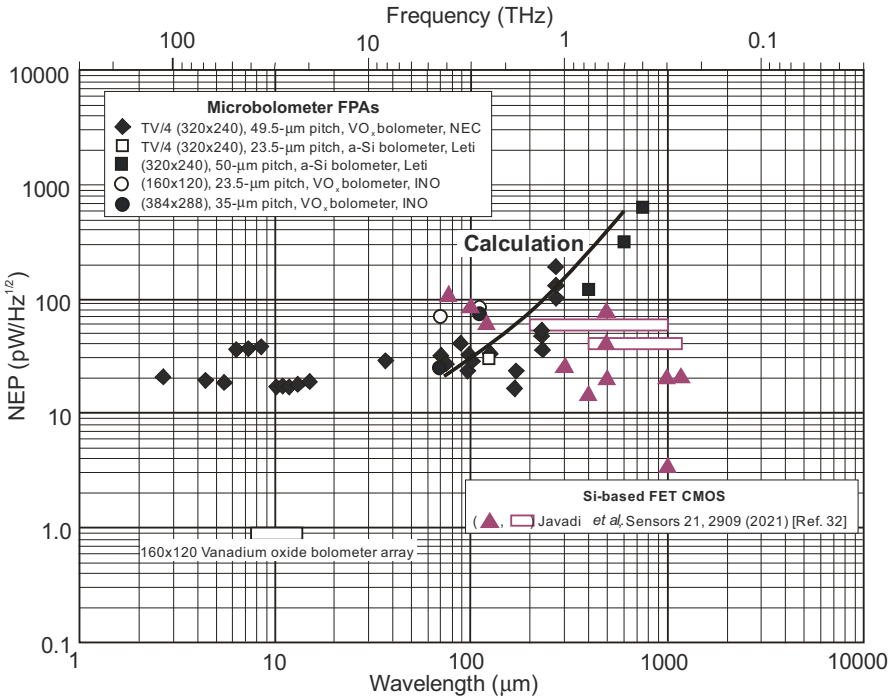

Fig. 5 NEP spectral dependence for Si-based FET CMOS detectors and microbolometer THz FPAs. The experimental data for Si-based FET CMOS detectors are taken from Ref. 32

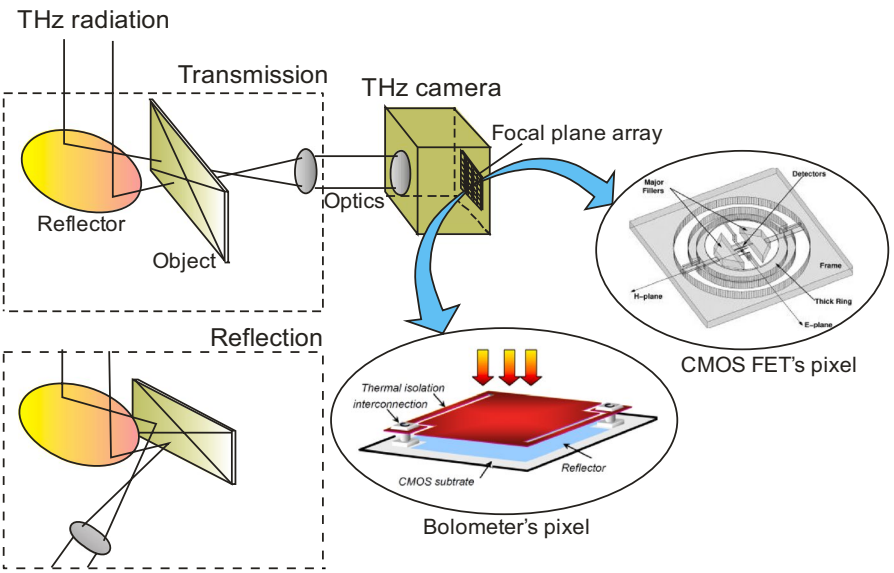

Fig. 6 Experimental setup of THz imaging system. Cutaway depicts alternative reflection mode setup (reprinted with permission from Rogalski [35])

the modified reflection mode setup, where a specular reflection is collected by the repositioned lens and camera.

In the period 2010–2011, three different companies/organizations announced cameras optimized for the > 1-THz frequency range: NEC (Japan) [36], INO (Canada) [37], and Leti (France) [38]. Several vendors fabricated cameras with array size from 16×16 to 384×288 pixels which is listed in Table 5 [39]. The largest and most sensitive ones are provided by microbolometer technology-based sensors. Their minimum detectable power (MDP) is in the range of a few dozen pW (at frequency a few THz). For comparison, the MDPs of FET-based cameras are in nW range, e.g., 9 nW for Tic-Wave camera developed by the University of Wuppertal. FET-based cameras are smaller and, due to larger footprints, are more suitable for longer wavelength range, up to100 GHz. Sensitivity of NeTHIS and Ophir Photonics cameras is considerably lower, around 10 μW, but their spectral response is very broad from infrared to terahertz. The first of them is thermo-conversion membrane-based camera. The second one contains hybrid array which consists of a $LiTaO_3$ pyroelectric crystal connected with indium bumps to a silicon readout multiplexer.

Figure 7 presents development status of commercial THz cameras containing two-dimensional detector arrays. Their details characteristics are given in Table 5.

Figure 8 presents trends in development of room-temperature 32×32 FET CMOS THz detectors. As can be seen, in the last 10 years, the *NEP* value has been improved by two orders of magnitude. The lowest reported *NEP* is in the range of 12–14 pW/$\sqrt{\text{Hz}}$ at operating band around 650–1000 GHz in 65-nm CMOS [46]. It should be noted that although device scaling may result in lower thermal noise of the MOSFET channel, the detector parameters (sensitivity, *NEP*, operating bandwidth) reported so far have not been significantly improved by migration to nanometer CMOS technology nodes. It is expected that one of the main possible reasons for this is the very high (in the kΩ range) and frequency-dependent impedance of the MOSFET operating in moderate inversion, which makes efficient and broadband coupling to the on-chip antenna very difficult.

6 Conclusions

Over the past 20 years, there have been significant technological developments that have enabled real-time high-resolution THz imaging. Today, THz imaging research is gradually being transferred from laboratory instruments to commercial products. Intensive research is being conducted to develop THz cameras similar to those available in the infrared spectrum. The technical requirements for THz cameras are the possibility of mass production, compatibility with standard fabrication technologies (e.g., CMOS process), low weight, small size and low-power consumption, and high sensitivity when operating at room temperature (allowing THz imaging even without an active THz source).

To realize THz cameras that meet these criteria, mainly two main technology directions are being pursued: THz thermal cameras and FET-based THz cameras. In particular, microbolometers have achieved remarkable sensitivity at room

Table 5 Commercial uncooled THz imaging cameras (reproduced from Simoens [40])

Camera – company	Sensor	Spectral range	Optics	Sensitivity
TZCAM – i2S http://www.i2s.fr/project/camera-terahertz-tzcam/	320×240 a-Si microbolometer 50 µm pitch LETI is the provider of the sensor	0.6–3 THz 25 fps	*f*/0.8, 50 mm focal plane	20–30 pW/pixel
IR/V-T0831 – NEC* http://www.nec.com/en/global/prod/terahertz/	320×240 VO_x microbolometer 23.5 µm pitch	1–7 THz 500 fps	*f*/1, 28.2 focal plane	*NEP* = 100 pW
MICROXCAM-384I-THz – INO http://www.ino.ca/en/products/terahertz-camera-microxcam-384i-thz/	384×288 VO_x microbolometer 35 µm pitch	0.94–4.25 THz 50 fps	*f*/0.9 or *f*/0.7 HRFZ-Si 44 mm focal plane	20–30 pW/pixel
TicMOS-1px – Tic-Wave https://ticwave.com/index.php/shop/ticmos-1kpx	32×32 FET	0.1–4 THz 500 pfs	No optics	*NEP* = 100 pW
Tera-257/1024/2056 – Terasense http://terasense.com/products/sub-thz-imaging-cameras/	16×16/32×32/64×64 FET 1.5 mm pitch	10 GHz-0.7 THz	No optics	14 nW (at 100 fps)
Pyrocam IV – Ophir Photonics http://www.ophiropt.com/laser--measurement/beam-profilers/products/Beam-Profiling/Camera-Profilingwith-BeamGage/Pyrocam-IV	320×240 pyroelectric 80 µm pitch	13–1355 nm, 1.06–3000 µm 100 fps	No optics, window assembly with AR coating	13 $nW/Hz^{1/2}$/pixel (1 Hz)
Open View – NeTHIS http://nethis-thz.com/index.php/openview/	256×320, 170 µm pitch/512×640, 80 µm pitch based on THz to IR converter	0.1–3000 µm 1 kfps	No optics	50 $\mu W/cm^2$

*The Japanese company NEC has abandoned manufacturing its THz bolometer camera after several years of production.

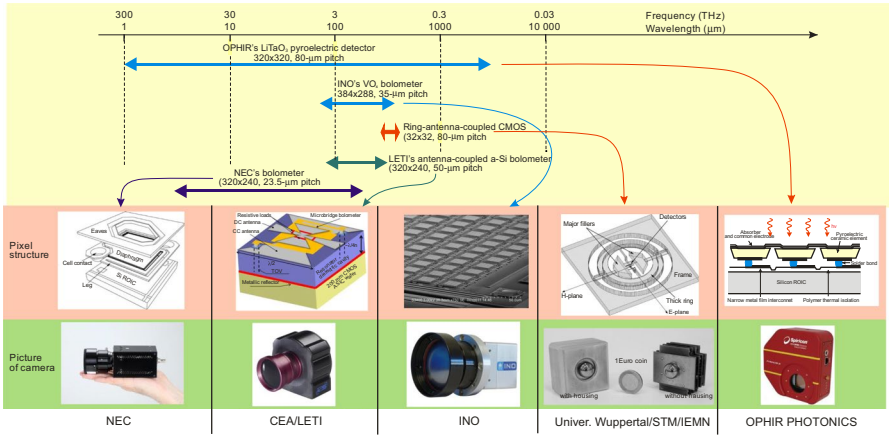

Fig. 7 Development status of uncooled THz focal plane arrays

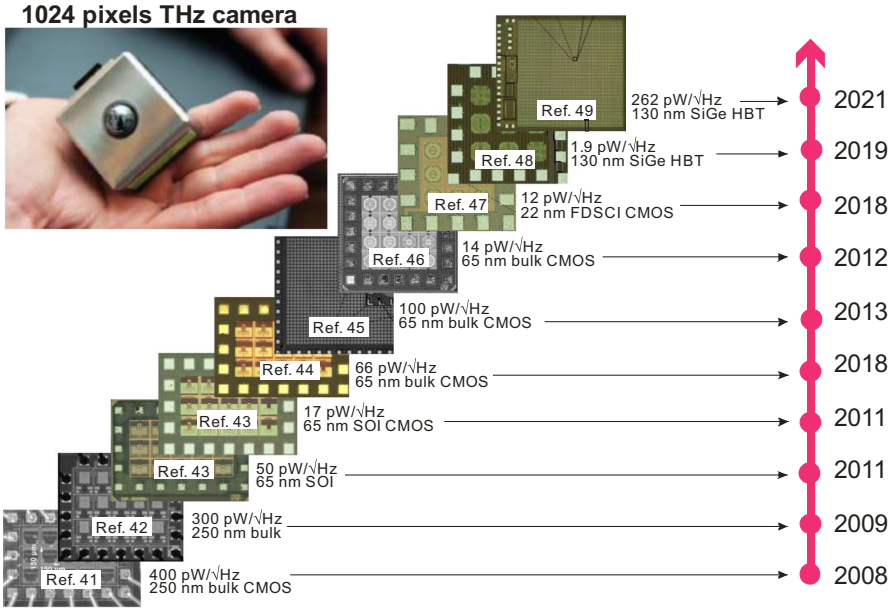

Fig. 8 Trends in development of room-temperature 32 × 32 FET CMOS THz detectors [41–49]

temperature by using a Fabry–Perot cavity, coupling antennas, and a meta-material absorber to increase the absorbed THz radiation. Cameras based on THz FET transistors measure the rectified voltage after interaction of THz radiation with the plasmon wave in the transistor channel. The silicon FET is an attractive candidate for a THz camera because it is compatible with CMOS technology, allowing scaling to high-resolution arrays at reduced cost.

The discovery of graphene and alternative 2D materials with direct energy gaps has opened a new window for THz photodetector fabrication. The combination of scalability, prospects for integration into Si-platforms, and the ability to implement flexible devices makes graphene competitive for the next generation of sensor systems. However, at the present stage of technology, 2D films have a small area (typically 100 μm^2), which makes it expensive for industrial applications. Moreover, this technology is not mature, which has detrimental influence on uniformity of pixel arrays. The development of efficient 2D photodetector arrays integrated in the focal plane of the imaging system is particularly critical in industrialization. Most experimental methods for transferring 2D materials from their substrate to the desired electronic circuits are either incompatible with high-volume production or lead to significant degradation of the 2D material and its electronic properties.

The above difficulties in scaling wafer sizes of 2D materials may be overcome in the future. In particular, this is already noticeable in the adaptation of 2D materials for the production of 2D transistors. For example, IMEC introduces tungsten disulfide (WS_2) in the logic device scaling roadmap [50]. Recently, the European Commission launched a 20 million project to bridge the gap between lab-scale manufacturing and large volume production of electronic devices based on 2D materials [51].

Funding This work was supported by the funds granted to the Faculty of Advanced Technologies and Chemistry, Military University of Technology, within the subsidy for maintaining research potential in 2021, grant no. UGB-842/2021.

Data Availability The data that support the findings of this study are available from the corresponding author upon reasonable request.

Declarations

Conflict of Interest The author declares no competing interests.

References

1. T. Robin and C. Bouye, "THz technologies offer varied options for industry", https://www.photonics.com/Articles/THz_Technologies_Offer_Varied_Options_for_Industry/a56089
2. M. Naftaly, N. Vieweg, and A. Deninger, "Industrial applications of terahertz sensing: State of play", *Sensors* **19**, 4203 (2019).
3. Tematys: Exploration of Photonics Markets. Available online: https://tematys.fr/Publications/en/terahertz/39-terahertz-components-systems-technology-and-market-trends-update-2016.html

4. QY Research. Available online: https://www.qyresearch.com/index/detail/1172368/global-terahertz-thztechnology-market
5. E.R. Brown and D. Segovia-Vargas, "Principles of THz direct detection", in *Semiconductor Terahertz Technology: Devices and Systems at Room Temperature Operation*, pp. 212–253, edited by G. Carpintero, L.E. Garcia Muñoz, L. Hartnagel, S. Preu, and A.V. Räisänem, Wiley, 2015.
6. A. Rogalski, *2D Materials for Infrared and Terahertz Detectors*, CRC Press, Boca Raton, 2021.
7. Y. Wang, W. Wu, and Z. Zhao, "Recent progress and remaining challenges of 2D material-based terahertz detectors", *Infrared Physics and Technology* **102**, 103024 (2019).
8. L. Viti, J. Hu, D. Coquillat, A. Politano, W. Knap, and M.S. Vitiello, "Efficient terahertz detection in black-phosphorus nano-transistors with selective and controllable plasma-wave, bolometric and thermoelectric response", *Sci. Rep*. **6**:20474 (2016).
9. W. Miao, H. Gao, Z. Wang, W. Zhang, Y. Ren, K.M. Zhou, S.C. Shi, C. Yu, Z.Z. He, Q.B. Liu, and Z.H. Feng, "A graphene-based terahertz hot electron bolometer with Johnson noise readout", *J. Low Temp. Phys*. **193**(3–4), 387–392 (2018).
10. A. El Fatimy, R.L. Myers-Ward, A.K. Boyd, K.M. Daniels, D.K. Gaskill, and P. Barbara, "Epitaxial graphene quantum dots for high-performance THz bolometers, *Nature Nanotechnology* **11**, 335–338 (2016).
11. X. Cai, A.B. Sushkov, R.J. Suess, M.M. Jadidi, G.S. Jenkins, L.O. Nyakiti, R.L. Myers-Ward, S. Li, J. Yan, D.K. Gaskill, T.E. Murphy, H.D. Drew, and M.S. Fuhrer, "Sensitive room-temperature terahertz detection via the photothermoelectric effect in graphene", *Nat. Nanotechnol*. **9**(10) 814–819 (2014).
12. J. Tong, M. Muthee, S.Y. Chen, S.K. Yngvesson, and J. Yan, "Antenna enhanced graphene THz emitter and detector", *Nano Lett*. **15**(8), 5295–5301 (2015).
13. L. Viti, J. Hu, D. Coquillat, W. Knap, A. Tredicucci, A. Politano, and M.S. Vitiello, "Black phosphorus terahertz photodetectors", *Adv. Mater*. **27**, 5567–5572 (2015).
14. L. Vicarelli, M.S. Vitiello, D. Coquillat, A. Lombardo, A.C. Ferrari, W. Knap, M. Polini, V. Pellegrini, and A. Tredicucci, "Graphene field-effect transistors as roomtemperature terahertz detectors", *Nat. Mater*. **11**(10), 865–871 (2012).
15. A. Zak, M.A. Andersson, M. Bauer, J. Matukas, A. Lisauskas, H.G. Roskos, and J. Stake, "Antenna-integrated 0.6 THz FET direct detectors based on CVD graphene", *Nano Lett*. **14**(10), 5834–5838 (2014).
16. D. Spirito, D. Coquillat, S.L. De Bonis, A. Lombardo, M. Bruna, A.C. Ferrari, V. Pellegrini, A. Tredicucci, W. Knap, and M.S. Vitiello, "High performance bilayer graphene terahertz detectors", *Appl. Phys. Lett*. **104**(6), 061111 (2014).
17. H. Qin, J. Sun, S. Liang, X. Li, X. Yang, Z. He, C. Yu, and Z. Feng, "Room-temperature, low-impedance and high-sensitivity terahertz direct detector based on bilayer graphene field-effect transistor", *Carbon* **116**, 760–765 (2017).
18. F. Bianco, D. Perenzoni, D. Convertino, S.L. De Bonis, D. Spirito, M. Perenzoni, C. Coletti, M.S. Vitiello, and A. Tredicucci, "Terahertz detection by epitaxial-graphene field-effect-transistors on silicon carbide", *Appl. Phys. Lett*. **10**(13), 131104 (2015).
19. D.A. Bandurin, I. Gayduchenko, Y. Cao, M. Moskotin, A. Principi, I.V. Grigorieva, G. Goltsman, G. Fedorov, and D. Svintsov, "Dual origin of room temperature sub-terahertz photoresponse in graphene field effect transistors", *Appl. Phys. Lett*. **112**(14), 141101 (2018).
20. L. Wang, C. Liu, X. Chen, J. Zhou, W. Hu, X. Wang, J. Li, W. Tang, A. Yu, S.-W. Wang, and W. Lu, "Toward sensitive room-temperature broadband detection from infrared to terahertz with antenna-integrated black phosphorus photoconductor", *Adv. Funct. Mater*. **27**(7), 1604414 (2017).
21. C. Liu, L. Wang, X. Chen, J. Zhou, W. Hu, X. Wang, J. Li, Z. Huang, W. Zhou, W. Tang, G. Xu, S.-W. Wang, and W. Lu, "Room-temperature photoconduction assisted by hot-carriers in graphene for sub-terahertz detection", *Carbon* **130**, 233–240 (2018).
22. X. Yang, A. Vorobiev, A. Generalov, M. A. Andersson, and J. Stake, "A flexible graphene terahertz detector", *Appl. Phys. Lett*. **111**, 021102 (2017).
23. A.A. Generalov, M.A. Andersson, X. Yang, A. Vorobiev, and J. Stake, "A 400-GHz graphene FET detector", *IEEE Trans. Terahertz Science & Technol*. **7**(5), 614-616 (2017).
24. C. Liu, L. Du, W. Tang, D. Wei, J. Li, L. Wang, G. Chen, X. Chen, and W. Lu, "Towards sensitive terahertz detection via thermoelectric manipulation using graphene transistors", *NPG Asia Materials* **10**, 318–327 (2018).
25. C. Liu, L. Wang, X. Chen, A. Politano, D. Wei, G. Chen, W. Tang, W. Lu, and A. Tredicucci, "Room-temperature high-gain long-wavelength photodetector via optical-electrical controlling of hot carriers in graphene", *Adv. Optical Mater.* 1800836 (2018).

26. G. Auton, D.B. But, J. Zhang, E. Hill, D. Coquillat, C. Consejo, P. Nouvel, W. Knap, L. Varani, F. Teppe, J. Torres, and A. Song, "Detection and imaging using graphene ballistic rectifiers", *Nano Lett*. **17**, 7015–7020 (2017).
27. L. Viti, D.G. Purdie, A. Lombardo, A.C. Ferrari, and M.S. Vitiello, "HBN-encapsulated, graphene-based, room-temperature terahertz receivers, with high speed and low noise", *Nano Lett*. **20**, 3169−3177 (2020).
28. S. Castilla, B. Terrés, M. Autore, L. Viti, J. Li,A.Y. Nikitin, I. Vangelidis, K. Watanabe, T. Taniguchi, E. Lidorikis, M.S. Vitiello, R. Hillenbrand, K.-J. Tielrooij, and F.H.L. Koppens, "Fast and sensitive terahertz detection using an antenna-integrated graphene pn junction", *Nano Lett*. **19**, 2765–2773 (2019).
29. W. Guo, L. Wang, X. Chen, C. Liu, W. Tang, C. Guo, J. Wang, and W. Lu, "Graphene-based broadband terahertz detector integrated with a square-spiral antenna", *Opt. Lett*. **43**, 1647–1650 (2018).
30. W. Guo, Z. Dong, Y. Xu, C. Liu, D. Wei, L. Zhang, X. Shi, C. Guo, H. Xu, G. Chen, L. Wang, K. Zhang, X. Chen, and W. Lu, "Sensitive terahertz detection and imaging driven by the photothermoelectric effect in ultrashort-channel black phosphorus devices", *Adv. Sci*. **7**, 1902699 (2020).
31. L. Viti, A. Politano, and M.S. Vitiello, "Black phosphorus nanodevices at terahertz frequencies: Photodetectors and future challenges", *APL Materials* **5**, 035602 (2017).
32. E. Javadi, D.B. But, K. Ikamas, J. Zdanevicius, W. Knap, and A. Lisauskas, "Sensitivity of field-effect transistor-based terahertz detectors", *Sensors* **21**, 2909 (2021).
33. J.O. Island, G.A. Steele, H.S.J. van der Zant, and A. Castellanos-Gomez, "Environmental instability of few-layer black phosphorus", *2D Mater.* **2**, 011002 (2015).
34. A. Rogalski, M. Kopytko, and P. Martyniuk, "2D material infrared and terahertz detectors: Status and outlook", *Opto-Electron. Rev.* **28**, 107-154 (2020).
35. A. Rogalski, "Far-infrared semiconductor detectors and focal plane arrys", in *THz and Security Applications*, edited by C. Corsi and F. Sizov, pp. 25-52, Springer, Dordrecht, 2014.
36. N. Oda, "Uncooled bolometer-type terahertz focal-plane array and camera for real-time imaging," *Comptes Rendus Physique* **11**, 496–509 (2010).
37. M. Bolduc, M. Terroux, B. Tremblay, L. Marchese, E. Savard, M. Doucet, H. Oulachgar, C. Alain, H. Jerominek, and A. Bergeron, "Noise-equivalent power characterization of an uncooled microbolometer-based THz imaging camera, *Proc. SPIE* **8023**, 80230C-1–10 (2011).
38. D.-T. Nguyen, F. Simoens , J.-L. Ouvrier-Buffet, J. Meilhan, and J.-L. Coutaz, "Broadband THz uncooled antenna-coupled microbolometer array—electromagnetic design, simulations and measurements . *IEEE Transactions on Terahertz Science and Technology* **2,** 299–305 (2012).
39. F. Simoens, J. Meilhan, L. Dussopt, J.-A. Nicolas, N. Monnier, G. Sicard, A. Siligaris, and B. Hiberty, "Uncooled terahertz real-time imaging 2D arrays developed at LETI: present status and perspectives", *Proc. SPIE* **1019**4, 101942N (2017).
40. F. Simoens, "Buyer's guide for a terahertz (THz) camera", *Photoniques Special EOS Issue* **2**, 58-62, March/April 2018.
41. U. Pfeiffer and E. Ojefors. "A 600-GHz CMOS focal-plane array for terahertz imaging applications", *European Solid-State Circuits Conf*., pp. 110–113 (2008).
42. E. Ojefors, A. Lisauskas, D. Glaab, H. G. Roskos, and U. R. Pfeiffer. "Terahertz imaging detectors in CMOS technology". In: *Journal of Infrared, Millimeter, and Terahertz Waves* **30**, 1269–1280 (2009).
43. H. Sherry, R. Al Hadi, J. Grzyb, E. Ojefors, A. Cathelin, A. Kaiser, and U. Pfeiffer. "Lens-integrated THz imaging arrays in 65 nm CMOS technologies", *Radio Freq. Integr. Circuits Symp*. 1–4 (2011).
44. R. Al Hadi, H. Sherry, J. Grzyb, N. Baktash, Y. Zhao, E. Ojefors, A. Kaiser, A. Cathelin, and U. Pfeiffer. "A broadband 0.6 to 1 THz CMOS imaging detector with an integrated lens", *IEEE MTT-S International Microwave Symposium*, 1–4 (2011).
45. R. Al Hadi, H. Sherry, J. Grzyb, Y. Zhao, W. Forster, H.M. Keller, A. Cathelin, A. Kaiser, and U.R. Pfeiffer, "A 1 k-pixel video camera for 0.7–1.1 terahertz imaging applications in 65-nm CMOS", *IEEE Journal of Solid-State Circuits* 47.12, 2999–3012 (2012).
46. U. Pfeiffer, J. Grzyb, H. Sherry, A. Cathelin, and A. Kaiser. "Toward low-NEP room-temperature THz MOSFET direct detectors in CMOS technology", *38th International Conference on Infrared, Millimeter, and Terahertz Waves* (IRMMW-THz), 1–2 (2013).
47. R. Jain, R. Zatta, J. Grzyb, D. Harame, and U.R. Pfeiffer. "A terahertz direct detector in 22 nm FD-SOI CMOS", *13th European Microwave Integrated Circuits Conference* (EuMIC), 25–28 (2018).
48. M. Andree, J. Grzyb, R. Jain, B. Heinemann, and U.R. Pfeiffer. "A broadband dual-polarized terahertz direct detector in a 0.13-µm SiGe HBT technology", *IEEE MTT- S International Microwave Symposium* (IMS), 500–503 (2019).

49. R. Jain, P. Hillger, J. Grzyb, and U.R. Pfeiffer. "A 32×32 pixel 0.46-to-0.75 THz light-field camera SoC in 0.13µm CMOS", *IEEE Int. Solid-State Circuits Conf.* (2021).
50. https://www.imec-int.com/en/articles/imec-shows-excellent-performance-in-ultra-scaled-fets-with-2d-material-channel
51. https://compoundsemiconductor.net/article/112712/Scaling_Up_Large-area_Integration_Of_2D_Materials